nature materials

ARTICLES

PUBLISHED ONLINE: 4 APRIL 2016 | DOI: 10.1038/NMAT4604

Proximate Kitaev quantum spin liquid behaviour in a honeycomb magnet

A. Banerjee[1]*, C. A. Bridges[2], J.-Q. Yan[3,4], A. A. Aczel[1], L. Li[5], M. B. Stone[1], G. E. Granroth[1,6], M. D. Lumsden[1], Y. Yiu[5], J. Knolle[7], S. Bhattacharjee[8,9], D. L. Kovrizhin[7], R. Moessner[8], D. A. Tennant[10], D. G. Mandrus[3,4] and S. E. Nagler[1,11]*

Quantum spin liquids (QSLs) are topological states of matter exhibiting remarkable properties such as the capacity to protect quantum information from decoherence. Whereas their featureless ground states have precluded their straightforward experimental identification, excited states are more revealing and particularly interesting owing to the emergence of fundamentally new excitations such as Majorana fermions. Ideal probes of these excitations are inelastic neutron scattering experiments. These we report here for a ruthenium-based material, α-$RuCl_3$, continuing a major search (so far concentrated on iridium materials) for realizations of the celebrated Kitaev honeycomb topological QSL. Our measurements confirm the requisite strong spin–orbit coupling and low-temperature magnetic order matching predictions proximate to the QSL. We find stacking faults, inherent to the highly two-dimensional nature of the material, resolve an outstanding puzzle. Crucially, dynamical response measurements above interlayer energy scales are naturally accounted for in terms of deconfinement physics expected for QSLs. Comparing these with recent dynamical calculations involving gauge flux excitations and Majorana fermions of the pure Kitaev model, we propose the excitation spectrum of α-$RuCl_3$ as a prime candidate for fractionalized Kitaev physics.

Exotic physics associated with frustrated quantum magnets is an enduring theme in condensed matter research. The formation of quantum spin liquids (QSLs) in such systems can give rise to topological states of matter with fractional excitations[1–4]. Fractionalization describes the counterintuitive phenomenon where an electron breaks apart into well-defined independent quasiparticles. The realization of this physics in real materials is an exciting prospect that may provide a path to a robust quantum computing technology[5]. Fractional excitations in the form of pairs of $S=1/2$ spinons are observed in quasi-one-dimensional (1D) materials containing $S=1/2$ Heisenberg antiferromagnetic chains[6]. Recent evidence for the 2D QSL state, in the form of possible spinon excitations, has been found in quantum antiferromagnets on triangular[3] and Kagome[7] lattices. The exactly solvable Kitaev model on the honeycomb lattice[8] represents a class of 2D QSL that supports two different emergent fractionalized excitations: Majorana fermions and gauge fluxes[9,10]. The comparatively simple gauge flux can be visualized as a spin–orbit coupled version of a plaquette observable like a resonance energy. The Majorana fermions, by contrast, do not have a straightforward real-space representation because they are not associated with any real-space spin or charge density. At best, an idea of their nature can be gleaned in the strongly anisotropic limit of weakly coupled Ising dimers, where they can be thought of as excitations taking the form of a misaligned nearest-neighbour spin pair on top of a ground state consisting of a coherent superposition of satisfied dimers. How to observe such ephemeral entities is one of the central challenges of condensed matter and materials physics today. It has turned out that the signature of the Majorana fermion in the response function measured by means of inelastic neutron scattering is perhaps one of the most direct ways of pinning down the excitation's existence[10]. This manuscript reports precisely such a measurement.

The Kitaev model consists of a set of spin-1/2 moments $\{\mathbf{S}_i\}$ arrayed on a honeycomb lattice. The Kitaev couplings, of strength K in equation (1), are highly anisotropic with a different spin component interacting for each of the three bonds of the honeycomb lattice. In actual materials, a Heisenberg interaction (J) is also generally expected to be present, giving rise to the Heisenberg–Kitaev (H–K) Hamiltonian[11,12].

$$H=\sum_{i,j}\left(KS_i^mS_j^m+J\mathbf{S}_i\cdot\mathbf{S}_j\right) \quad (1)$$

where m is the component of the spin directed along the bond connecting spins (i,j). The QSL phase of the pure Kitaev model ($J=0$), for both ferromagnetic and antiferromagnetic K, is stable for weak Heisenberg perturbations.

Remarkably, the Hamiltonian (1) has been proposed to accurately describe edge-shared octahedrally coordinated magnetic systems, shown in Fig. 1a, with dominant spin–orbit coupling[11,12].

[1]Quantum Condensed Matter Division, Oak Ridge National Laboratory, Oak Ridge, Tennessee 37830, USA. [2]Chemical Sciences Division, Oak Ridge National Laboratory, Oak Ridge, Tennessee 37830, USA. [3]Material Sciences and Technology Division, Oak Ridge National Laboratory, Oak Ridge, Tennessee 37830, USA. [4]Department of Materials Science and Engineering, University of Tennessee, Knoxville, Tennessee 37996, USA. [5]Department of Physics, University of Tennessee, Knoxville, Tennessee 37996, USA. [6]Neutron Data Analysis & Visualization Division, Oak Ridge National Laboratory, Oak Ridge, Tennessee 37830, USA. [7]Department of Physics, Cavendish Laboratory, J.J. Thomson Avenue, Cambridge CB3 0HE, UK. [8]Max Planck Institute for the Physics of Complex Systems, D-01187 Dresden, Germany. [9]International Center for Theoretical Sciences, TIFR, Bangalore 560012, India. [10]Neutron Sciences Directorate, Oak Ridge National Laboratory, Oak Ridge, Tennessee 37830, USA. [11]Bredesen Center, University of Tennessee, Knoxville, Tennessee 37966, USA. *e-mail: banerjeea@ornl.gov; naglerse@ornl.gov

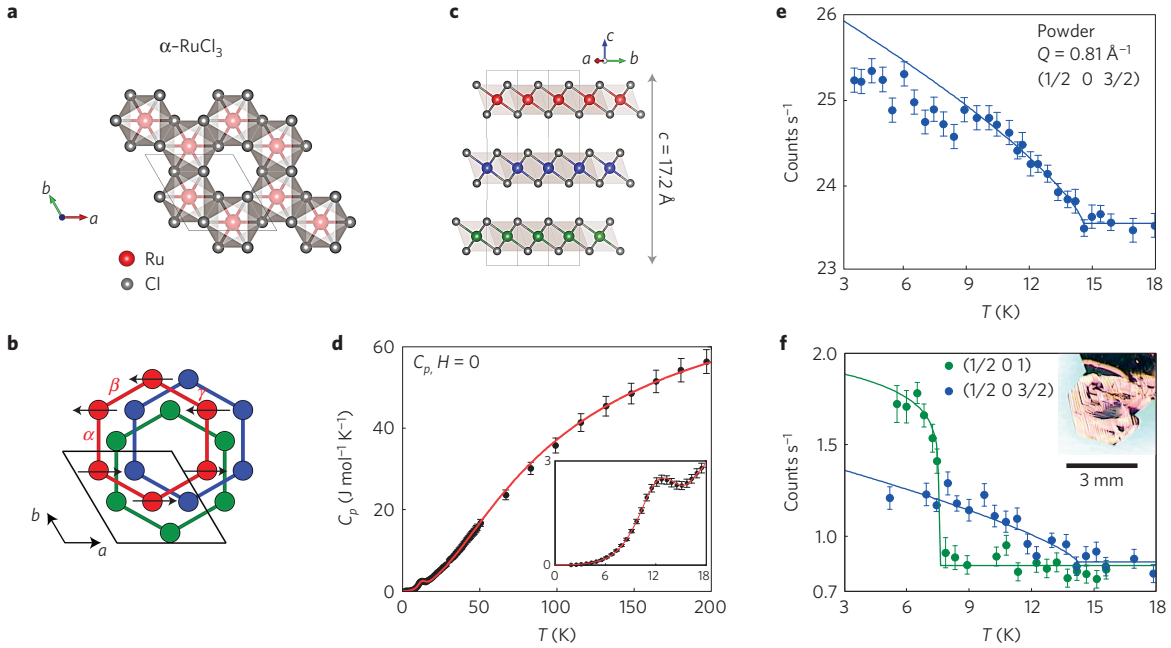

Figure 1 | Structure and bulk properties of 2D layered α-$RuCl_3$. a–c, The structure of α-$RuCl_3$ (space group no. 151, $P3_112$). **a**, In-plane honeycomb structure showing edge-sharing $RuCl_6$ octahedra and the unit cell of the honeycomb lattice. **b**, View along the *c* axis showing the stacking of honeycomb layers in the unit cell, with Ru atoms in each layer denoted by the colours red, blue or green. The different intralayer Ru–Ru bonds, corresponding to the index '*m*' in equation (1), are labelled in the red layer as α, β, or γ, each with distance $a/\sqrt{3}$. The 2D zigzag magnetic structure is illustrated by the black spins on the red layer. **c**, Side view of the unit cell showing the offsets along the *c* axis. Values noted are for room-temperature lattice constants. **d**, Specific heat of powder α-$RuCl_3$. The solid red line is a fit of the data following the 2D Debye model $C_p(T) = ANk(T/\theta_D)^2 \int_0^{\theta_D/T} (x^2/e^x - 1)dx$ for $T > 16$ K, and for $T < 16$ K an empirical function describing the anomaly associated with magnetic order. The inset in **d** shows a close-up of the anomaly associated with the low-temperature magnetic ordering transition at $T_N \approx 14$ K in powder samples. (See Supplementary Fig. 1 for more details of thermodynamic measurements.) The error bars include statistical and systematic uncertainties of the physical property measurement system (PPMS) measurement. **e**, Order parameter plot of the (1/2 0 3/2) magnetic Bragg peak ($Q = 0.81$ Å^{-1}) in powder samples measured using neutron diffraction (see Methods). The solid blue line is a power-law fit to the data above 9 K, yielding $T_N = 14.6(3)$ K, with $\beta = 0.37(3)$. **f**, Similar plot for single crystals showing two coexisting ordering wavevectors (1/2 0 1), with $T_{N1} = 7.6(2)$ K (green), and (1/2 0 3/2), with $T_{N2} = 14.2(8)$ K (blue). Note that the (1/2 0 1) peak loses intensity sharply, as compared to the (1/2 0 3/2) peak. Inset: picture of the single crystal (22.5 mg) used in these measurements. Signals in **e**,**f**, are normalized to counts s^{-1} and the error bars represent 1 s.d. (σ), assuming Poisson counting statistics.

The focus so far has centred largely on Ir^{4+} compounds[13–19]; however, attempts to measure the dynamical response[15] by means of inelastic neutron scattering (INS) have met with limited success, owing to the unfavourable magnetic form factor and strong absorption cross-section of the Ir ions. Resonant inelastic X-ray scattering (RIXS) has provided important information concerning higher-energy excitations in the iridates[18], but cannot provide the meV energy resolution necessary to provide a robust experimental signature of collective fractional excitations that are expected to occur at energy scales of the order of 1–10 meV (ref. 15).

An alternative approach is to explore materials with Ru^{3+} ions[20]. The realization that the material α-$RuCl_3$ (refs 20–22) also has the requisite honeycomb lattice and strong spin–orbit coupling has stimulated a groundswell of recent investigations[23–29]. Although these studies lend support to the material as a potential Kitaev material, conflicting results centring on the low-temperature magnetic properties have hindered progress. To resolve this, we undertake a comprehensive evaluation of the magnetic and spin–orbit properties of α-$RuCl_3$, and further measure the dynamical response, establishing this material as proximate to the widely sought QSL.

We begin by investigating the crystal and magnetic structure of α-$RuCl_3$. Samples were synthesized and characterized as described in Methods. The layered structure of the material is shown in Fig. 1a. Figure 1b,c shows the ABCABC stacking arrangement of the layers expected in the trigonal structure (space group $P3_112$). That the layers are weakly bonded to each other, similar to graphite, is demonstrated by the lattice specific heat (shown for a powder in Fig. 1d). This exhibits a tell-tale T^2 behaviour characteristic of highly 2D bonded systems[30], rather than the usual T^3 observed in conventional 3D solids. Because the 2D layers are weakly coupled, the interlayer magnetic exchanges will also be rather weak. In addition, stacking faults are formed easily and significant regions of the sample can crystallize in alternative stacking structures, for example ABAB (ref. 25) (see Supplementary Fig. 2).

Neutron diffraction (see Methods) shows low-temperature magnetic order. The temperature dependence of the strongest magnetic powder peak, with $T_N \approx 14$ K, is shown in Fig. 1e. Figure 1f shows the temperature dependence of magnetic peaks in one 22.5 mg single crystal, revealing two ordered phases. The first, which orders below $T_N \approx 14$ K, is characterized by a wavevector $\mathbf{q}_1 = (1/2\ 0\ 3/2)$ (indexed according to the trigonal structure), whereas the other phase ($\mathbf{q}_2 = (1/2\ 0\ 1)$) orders below 8 K (see also Supplementary Fig. 3). These temperatures correspond precisely to anomalies observed in the specific heat and magnetic susceptibility[25,26,29] (Supplementary Fig. 1). This is readily explained, as the observed $L = 3/2$ phase corresponds naturally to a stacking order of ABAB type along the *c*-axis, and the $L = 1$ corresponds to ABCABC stacking. Indeed, the difference in 3D transitions is a residual effect of different interlayer bonding influencing the ordering. Further, a comparison of intensities at (1/2 0 L) with (3/2 0 L)[16] shows both phases share identical zigzag (ZZ) spin ordering in the honeycomb layers; a phase of the H–K model adjacent to the spin liquid[11] (see Supplementary Table 1).

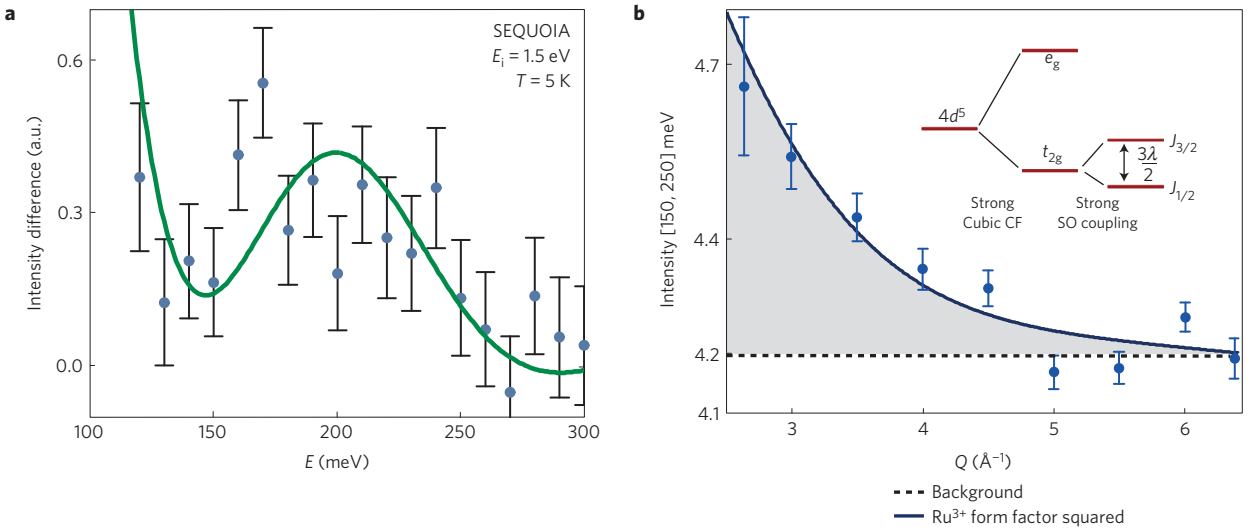

Figure 2 | Spin-orbit coupling mode in α-$RuCl_3$, measured using inelastic neutron scattering at $T = 5$ K with incident energy $E_i = 1.5$ eV. a, Difference between data integrated over the ranges $Q = [2.5, 4.0]$ Å^{-1} and [4.5, 6.0] Å^{-1} shown in Supplementary Fig. 4, subtracted point by point, illustrating the enhanced signal at low Q. The solid line is a fit to a background plus a Gaussian peak centred at 195 ± 11 meV with HWHM 48 ± 6 meV. With the settings used for the measurement, the width is resolution limited. Error bars represent 1σ (see Methods). **b**, Intensity for various values of wavevector integrated over the energy range [150, 250] meV (each point represents a summation in Q over 0.5 Å^{-1}, except for the first point, which is over 0.26 Å^{-1}). The solid line shows a two-parameter fit of the data to the equation $A\left|f^{\mathrm{mag}}(Q)\right|^2 + B$, where $f^{\mathrm{mag}}(Q)$ is the Ru^{3+} magnetic form factor in the spherical approximation. The shaded area represents the contribution arising from magnetic scattering. Inset: a schematic of the single-ion energy levels for d^5 electrons in the strong octahedral field (that is, low spin) limit with spin–orbit coupling showing the $J_{1/2}$ to $J_{3/2}$ transition at energy $3\lambda/2$.

By calibrating to structural Bragg peaks, the ordered moments are measured to be exceptionally low, with an upper bound of $\mu = 0.4 \pm 0.1\mu_B$. This is at most only 35% of the full moment determined from bulk measurements[22,25,27], suggesting strong spin fluctuations consistent with a near-liquid-like quantum state in the material. (See Supplementary Information for more detail.)

Having established the structural and magnetic properties of α-$RuCl_3$, we probe the nature of the single-ion states to confirm the presence of strong spin–orbit coupling, which is required to generate the Kitaev term K in equation (1). Using INS (see Methods) with $E_i = 1.5$ eV incident neutrons to measure the transition from the Ru^{3+} electronic ground state to its excited state, the spin–orbit coupling λ is extracted. In the octahedral environment shown in Fig. 1, the ground state is a low-spin ($J = 1/2$) state. The next excited state ($J = 3/2$) is separated by $3\lambda/2$. Neutrons can activate it by a spin-flip process, and the transition is seen in Fig. 2 at 195 ± 11 meV, implying that $\lambda \approx 130$ meV (also see Supplementary Fig. 4 and Supplementary Information). This is close to the expected free-ion value ($\lambda_{\mathrm{free}} \approx 150$ meV; refs 20,31) and the predictions of recent *ab initio* calculations[26]. The $J = 3/2$ state will be split into two Kramers doublets by small distortions of the octahedron[32,33]. The resolution-limited linewidth suggests that such a splitting is relatively small, certainly less than the half-width at half-maximum (HWHM) of 48 meV. In any case, as the higher levels are too energetic to play any role, only the lowest lying doublet needs to be considered. Projecting the inter-Ru^{3+} couplings into this doublet results in Kitaev terms as included in equation (1).

The above results indicate that the H–K Hamiltonian (1) can indeed satisfactorily capture the interactions between Ru^{3+} moments. If this is the case, then given the highly reduced ordered moment and the extended QSL region close to the observed zigzag AFM phase, it is tempting to speculate that signatures of fractionalization characteristic of QSLs will be manifest in the collective magnetic excitations. Figure 3 shows INS data for α-$RuCl_3$ powder measured using neutrons of $E_i = 25$ meV (more details in Methods). The scattering in the magnetically ordered state is shown in Fig. 3a for $T = 5$ K. Two distinct features are clearly visible, spanning different energy ranges. The lower among them, M_1, is centred near 4 meV and shows a minimum near $Q = 0.62$ Å^{-1}, which notably corresponds to the M point of the honeycomb lattice, as expected for a quasi-2D magnetic system (for 3D behaviour a wavevector $Q = 0.81$ Å^{-1} is anticipated). The white arrow draws attention to the concave shape of the edge of the scattering, which is expected for magnon excitations in a ZZ ordered state[15]. This firmly establishes the nature of magnetic order and differentiates it from other potential states, such as a stripy ground state. The second feature is at a higher energy, M_2, centred near 6.5 meV.

Both features, M_1 and M_2, correspond to powder-averaged modes which are of magnetic origin, as identified by their wavevector and temperature dependence. The thermal behaviour of these magnetic modes differs significantly from one to the other. Figure 3b shows the scattering at $T = 15$ K, just above T_N. It is seen that M_1 softens markedly and the intensity shifts towards $Q = 0$. Conversely, M_2 is essentially unaffected. Constant-Q cuts through the data are shown in Fig. 3c. The centres are at the positions indicated by the labelled dashed lines in Fig. 3a,b. Comparing cuts (A,B) with (C,D) reinforces the collapse and shift of intensity for M_1 above T_N. Cut B clearly shows two peaks, implying that the density of states sampled by the powder average at $T = 5$ K has two maxima. The average peak energies determined by fits of the data to Gaussian peaks are given by $E_1 = 4.1(1)$ meV and $E_2 = 6.5(1)$ meV. Figure 3d shows constant-energy cuts integrated over the range [2.5, 3.0] meV, near the lower edge of M_1. It is seen that, at low temperature, M_1 is structured with low-energy features showing up as peaks in cut E. These are centred at $Q_1 = 0.62(3)$ Å^{-1} and $Q_2 = 1.7(1)$ Å^{-1}. Above T_N this structure disappears, and the broad scattering shifts markedly to lower Q. Fitting the $T = 15$ K data (cut F) to a Lorentzian with the centre fixed at $Q = 0$ yields a HWHM of roughly 0.6 Å^{-1}, suggesting that, above T_N, spatial correlations of the spin fluctuations are extremely short ranged.

To gain further insight into the magnetic couplings we compare the INS data to the solution of (1) using conventional linear spin wave theory (SWT) for ZZ order[34,35]. The SWT provides a quasi-classical approximation which works reasonably well when

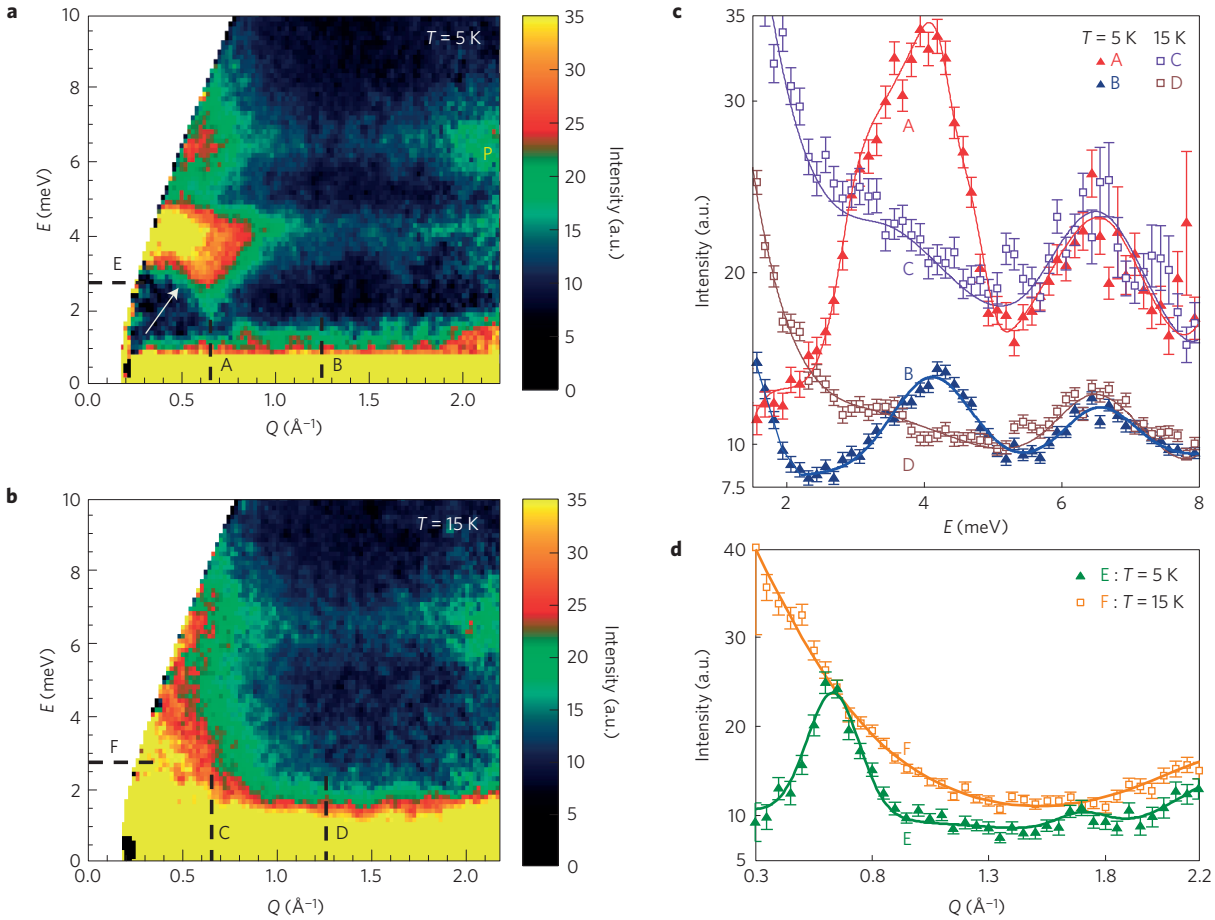

Figure 3 | Collective magnetic modes measured with inelastic neutron scattering using 25 meV incident neutrons. a, False colour plot of the data at $T = 5$ K showing magnetic modes (M_1 and M_2) with band centres near $E = 4$ and 6 meV. M_1 shows an apparent minimum near $Q = 0.62$ Å^{-1}, close to the magnitude of the M point of the honeycomb reciprocal lattice. The white arrow shows the concave lower edge of the M_1 mode. The yellow 'P' denotes a phonon that contributes to the scattering at an energy near that of M_2, but at higher wavevectors of $Q > 2$ Å^{-1}. **b**, The corresponding plot above T_N at $T = 15$ K shows that M_1 has disappeared, leaving strong quasi-elastic scattering at lower values of Q and E. **c**, Constant-Q cuts through the scattering depicted in **a** and **b** centred at wavevectors indicated by the dashed lines. The cuts A and C are summed over the range [0.5, 0.8] Å^{-1}, which includes the M point of the 2D reciprocal lattice, whereas B and D span [1.0, 1.5] Å^{-1}. The data from 2–8 meV in cut B is fitted (solid blue line) to a linear background plus a pair of Gaussians, yielding peak energies $E_1 = 4.1(1)$ meV and $E_2 = 6.5(1)$ meV. **d**, Constant-E cuts integrated over the energy range [2.5, 3.0] meV, at 4 K (E) and 15 K (F). See text for detail. The intensity in all four panels, including the colour bars, is reported in the same arbitrary units. In **c**,**d**, the solid lines through all the cuts A–F are guides to the eye. The error bars represent 1σ (see Methods).

quantum fluctuations are weak. Although strictly speaking it is inapplicable for strongly quantum fluctuating systems, it provides a first starting point for estimating the approximate and relative strengths of the couplings. In the honeycomb lattice appropriate for α-$RuCl_3$, SWT predicts four branches, two of which disperse from zero energy at the M point (1/2, 0) to doubly degenerate energies $\omega_1 = \sqrt{K(K+J)}$ and $\omega_2 = |J|\sqrt{2}$, respectively, at the Γ point (0,0) (ref. 34). A large density of states in the form of van Hove singularities is expected near ω_1 and ω_2. Figure 4a shows the SWT and Fig. 4b the calculated powder-averaged neutron scattering. Equating ω_1 and ω_2 with the peaks E_1 and E_2 yields K and J values of ($K = 7.0$, $J = -4.6$) meV (shown in Fig. 4) or ($K = 8.1$, $J = -2.9$) meV (shown in Supplementary Fig. 5), depending on whether ω_1 corresponds to E_1 or E_2. These two possibilities lie on either side of the symmetric point $K = -2J$, where $\omega_1 = \omega_2$. The inset of Fig. 4d shows each of these possibilities on the H–K phase diagram[34]. Either way, the Kitaev term is stronger and antiferromagnetic, whereas the Heisenberg term is ferromagnetic; again consistent with *ab initio* calculations[26].

We note that the M_1 mode has a gap of at least 1.7 meV near the M point (see Fig. 5a) that is not exhibited in the above SWT calculations. Although such a gapless spectrum is a known artefact of linear SWT for the H–K model[34], the experimentally observed gap is too large to be accounted for within systematic 1/S corrections. Extending the Hamiltonian to include further terms can lead to a gap forming within SWT. However, calculations of the SW spectrum (see Supplementary Fig. 5 and Supplementary Information) with additional terms in the Hamiltonian (such as Γ and/or Γ' terms[35–39]), when sufficient to generate the observed gap, show features in the powder-averaged scattering that are inconsistent with the observations. Within the SW approximation, a gap can also be generated by adding an additional Ising-like anisotropy, perhaps at the level of 15% of J, which is also equivalent to an anisotropic Kitaev interaction. As discussed below, the resulting SWT is still incompatible with the data.

Although the SWT calculation reproduces many of the features of the observed dynamical response, crucial qualitative disagreements remain. Most importantly, the observed dependence of the M_2 mode on temperature and energy is incompatible with linear SWT. The constant-wavevector cuts shown in Fig. 3c show that M_2 maintains a totally consistent peak shape and intensity above and below T_N. Moreover, for temperatures well above T_N, to at least 40 K, the

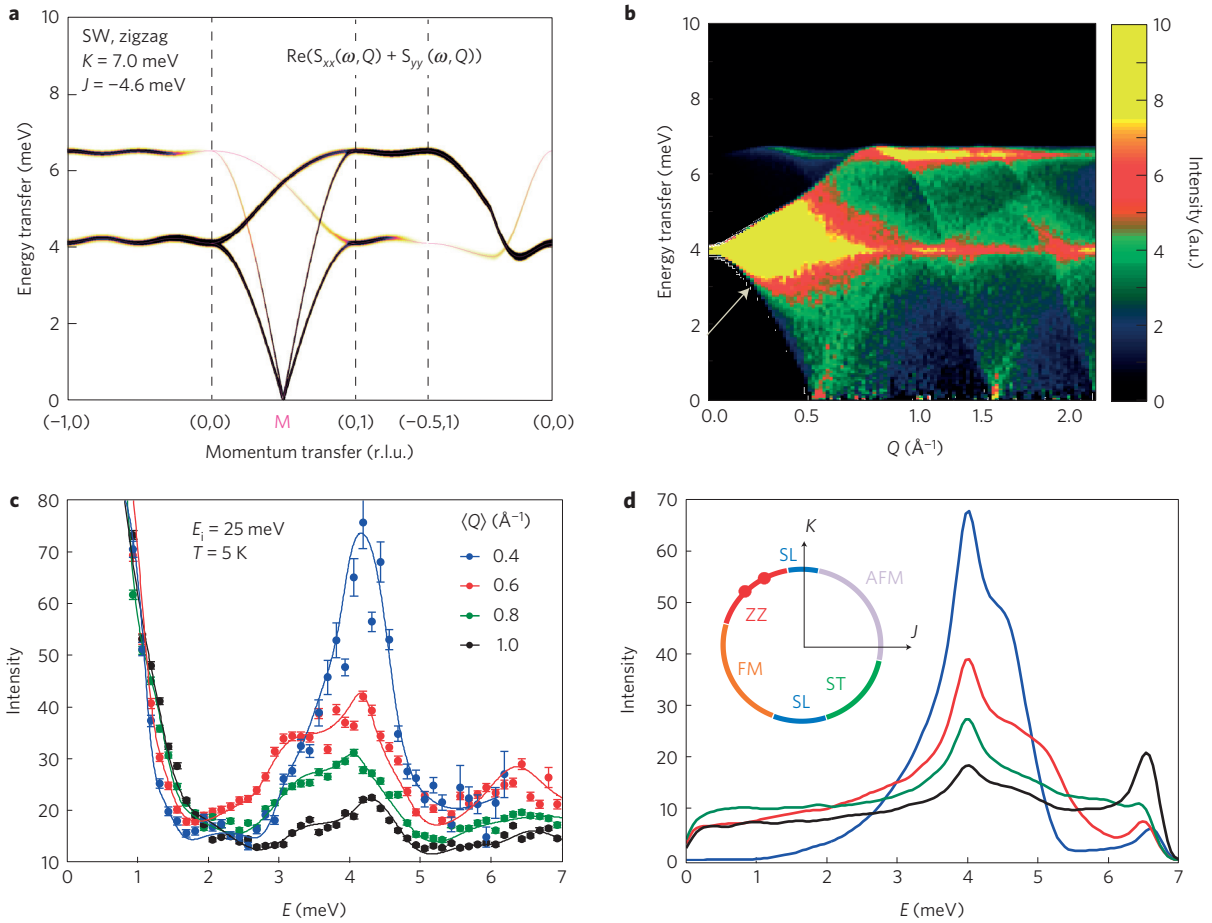

Figure 4 | Spin wave theory calculations. a, Spin wave simulation for the H–K model with $(K, J) = (7.0, -4.6)$ meV with a ZZ ground state. The lattice is the honeycomb plane appropriate for the $P3_112$ space group. **b**, The calculated powder-averaged scattering including the magnetic form factor. The white arrow shows the concave nature of the edge of the lower mode in (Q, E) space, similar to the data in Fig. 3a. **c**, Cuts through the data of Fig. 3a integrated over 0.2 Å^{-1} wide bands of wavevector centred at the values shown. Lines are guides to the eye. Note that actual data include a large elastic response from Bragg and incoherent scattering at $E = 0$ meV. The error bars represent 1σ. **d**, The same cuts, through the calculated scattering shown in Fig. 4b. Inset: phase diagram of the H–K model, after ref. 33. The various phases are denoted by different colours: spin liquid (SL, blue), antiferromagnetic (AFM, light violet), stripy (ST, green), ferromagnetic (FM, orange) and zigzag (ZZ, red). The red dots represent the two solutions for α-$RuCl_3$ as determined by the zone-centre spin wave mode energies.

intensity for all measured wavevectors is essentially unchanged, as shown by Fig. 5b, which is a plot of the M_2 intensity as a function of Q for several temperatures. In fact a well-defined M_2 peak persists with a similar Q dependence up to at least 70 K, corresponding to $T \sim 5T_N$. This is in sharp contrast to the typical behaviour of spin waves in conventional magnets, which generally exhibit a pronounced decrease of intensity above the ordering temperature. It should also be noted that in the ordered state the energy width of M_2 is much broader than the SW calculation over the observed range of Q. Figure 5c shows a constant-Q cut around the M_2 mode (blue triangles). The red line shows the equivalent powder-averaged SWT calculation (Fig. 4b), broadened by the instrumental energy resolution (marked 'R') and scaled so that the intensity matches the height of the M_2 scattering. The low-energy side of the calculation is affected by the lower mode, and therefore cannot be directly compared with the data; however, it is clear from the high-energy side that there is considerable extra scattering (indicated by the shading) that is not captured by SWT. As discussed in the Supplementary Information, the smooth drop off of intensity on the high-energy side of the M_2 peak is evidence against the extra width arising from additional features in the spin wave spectrum that can be achieved by adding extra terms to equation (1). Finally, as discussed in the Supplementary Information, for temperatures above T_N, the detailed wavevector dependence of the scattering is not what is expected from conventional SWT.

The SWT is a quantization of harmonic excitations from classical order. Moreover, the low-ordered moment observed in α-$RuCl_3$ indicates that linear SWT is inadequate. Indeed, we argue that the behaviour of the observed higher-energy mode M_2—which because of its short timescale is least sensitive to 3D couplings—is naturally accounted for through the QSL phase proximate in the H–K phase diagram[40].

This QSL viewpoint has the strong quantum limit as its starting point. It can avail itself of the recently computed exact dynamical structure factor of the pure Kitaev model, in which spin excitations fractionalize into static Ising fluxes and propagating Majorana fermions minimally coupled to a Z_2 gauge field[10]. Powder-averaged results of the scattering[10] expected for the isotropic antiferromagnetic Kitaev model are shown in Fig. 5d. Although the QSL is gapless, the structure factor of its excitations shown in Fig. 5d does show a gap. This is due to the fact that a spin flip always excites both quasiparticles—gapless Majorana fermions and a pair of Ising fluxes, the latter with a non-zero excitation gap[10]. This results in a low-energy band from 0.125 to 0.5 K, with a peak of intensity near the M point in the Brillouin zone for an antiferromagnetic K. Most interestingly, in addition, a second very broad and

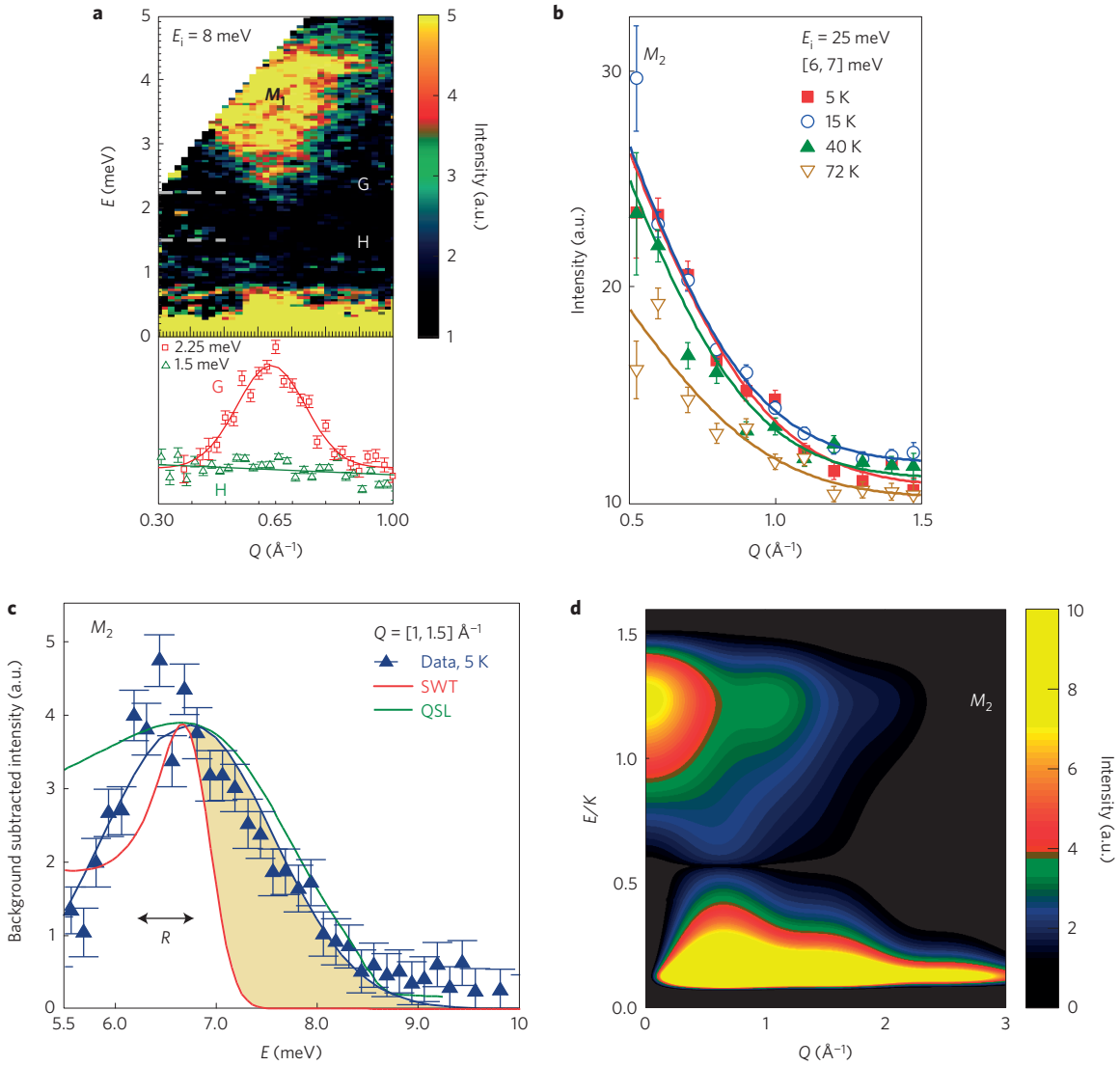

Figure 5 | Disagreements with classical SWT and agreement with QSL calculations. a, Scattering from mode M_1 measured using INS at $T = 5$ K using $E_i = 8$ meV. Lower panel shows constant-energy cuts over the energy ranges shown, centred at the locations labelled (G,H) in the upper panel. The absence of structured scattering below 2 meV confirms the gap in the magnetic excitation spectrum. **b**, Constant-E cuts of the data through the upper mode at four different temperatures, of which one curve at $T = 5$ K is below T_N (red squares) and rest above T_N. The lines are guides to the eye. **c**, A constant-Q cut of the $E_i = 25$ meV, $T = 5$ K data in the Q range shown. The blue triangles show the M_2 portion of the cut B in Fig. 3c, but with the linear background term subtracted, and the blue line is a fit to a Gaussian peak. As discussed in the text, the red line shows simulated SWT scattering and the green line shows the scattering calculated from a Kitaev QSL response function. The shaded area represents magnetic scattering that is not captured by the SWT. The double-ended arrow marked 'R' shows the full-width at half-maximum (FWHM) of the instrumental resolution of 0.5 meV at 6.5 meV. In panels **a**–**c**, the error bars represent 1σ (see Methods). **d**, The powder-averaged scattering calculated from a 2D isotropic Kitaev model, with antiferromagnetic K, using the results of ref. 10, including the magnetic form factor. The upper feature is broad in energy and decreases in strength largely monotonically as Q increases.

non-dispersing high-energy band appears, centred at an energy that corresponds approximately to the Kitaev exchange scale, K. (For a similar calculation on the ferromagnetic Kitaev model, and a general discussion, see Supplementary Fig. 6 and Supplementary Information) The intensity of the upper band is strongest at $Q = 0$, and decreases with increasing Q.

With the Kitaev interaction dominant it is reasonable to expect that α-$RuCl_3$ is proximate to the QSL phase. The additional non-Kitaev interactions lead to long-range order at low temperatures, and strongly affect the low-energy excitations, which then exhibit spin wave behaviour. Conversely, the high-energy spin fluctuations native to the proximate quantum ground state are more immune, and can persist even in the ordered state. This behaviour is well known in coupled $S = 1/2$ antiferromagnetic Heisenberg chains[6], where at energies large compared to the interchain coupling the spectrum of fractionalized excitations (spinons) of the pure chain dominates the response above and below the magnetic ordering temperature. This leads to a natural interpretation of the M_2 mode as having the same origin as the upper mode of the Kitaev QSL. The broad width of the M_2 mode as seen in the measurements can be naturally explained in terms of the fractionalized Majorana fermion excitations. The green line in Fig. 5c shows the calculated powder-averaged QSL scattering, including the effects of instrumental resolution, with the value $K = 5.5$ meV chosen to match the experimental peak position of M_2 and the overall height chosen to match the observed scattering. The calculated QSL scattering profile is well matched to the observed additional width of the M_2 scattering on the high-energy side. This value of K is slightly smaller than that inferred from SWT, but it is very reasonable to expect that the quantum description requires a renormalized parameter. The large

energy width is expected for a fractionalized system, because several excitations are excited in a single spin-flip process. Moreover, the Q dependence of the intensity of the M_2 mode (Fig. 5b) strikingly resembles that of the upper band in the pure Kitaev model. The feature is broad in momentum, because the real-space spin correlations of a QSL are short ranged. For convenience, a side-by-side comparison of the Q dependence of the data and the scattering calculated for SWT and a pure Kitaev model is presented in Supplementary Fig. 7.

The fact that M_2 survives well above T_N, even if M_1 is completely washed out, indicates that the M_2 mode is not directly connected to the existence of long-range magnetic order. In the strictly 2D Kitaev model there is no true phase transition from the QSL to the high-temperature paramagnet[41]. However, recent Monte Carlo calculations at finite temperature suggest that high-energy Majorana fermions, thus the M_2 mode, remain stable up to the highest crossover temperature at an energy scale of K (ref. 42), consistent with the observations reported here.

Taken together, the qualitative features from a complete quantum calculation using a Majorana fermion treatment can successfully provide a broadly consistent account of the inelastic neutron scattering data. This makes α-$RuCl_3$ a prime candidate for realizing Kitaev and QSL physics. Further support for the presence of Kitaev QSL physics in α-$RuCl_3$ is seen in recent Raman scattering measurements[24] which show a broad response similar to that calculated for the pure Kitaev model[17], with a value of $K = 8$ meV, of the same order as that derived here. The Raman continuum also persists to temperatures well above T_N. Much more detailed information on the structure of the response functions will require INS in single crystals of both α-$RuCl_3$ and other relevant compounds, some of which are 3D (refs 43,44). The most instructive measurements on α-$RuCl_3$ should use single crystals free of the complications induced by stacking faults.

Ideally, a single, fully quantum theoretical treatment should capture the microscopic behaviour across all energy and length scales; however, such a treatment is unavailable for the full Hamiltonian describing the magnetic properties of α-$RuCl_3$. Here, we have used the insight that the high-energy short-range spin-liquid physics is well captured by a pure Kitaev model, which permits an analytic treatment, but misses the weak ordering tendency owing to perturbations to the simple model Hamiltonian. These, however, and their concomitant low-energy spin wave excitations can be approximately captured by SWT. Considering the usual renormalizations inherent in semiclassical descriptions of quantum excitations, these two approximation schemes for different parts of the spectrum can be described by similar microscopic parameters, suggesting that the absence of a full treatment of the complete H–K model is a technical rather than a conceptual issue.

Looking forward, it will also be of great interest to systematically investigate the effects of disorder and doping in these materials[45], and there is also the hope of generating a genuinely 2D system by exfoliation techniques.

Methods

Methods and any associated references are available in the online version of the paper.

Received 11 August 2015; accepted 22 February 2016; published online 4 April 2016

References

1. Balents, L. Spin liquids in frustrated magnets. *Nature* **464,** 199–208 (2010).
2. Lee, P. A. An end to the drought of quantum spin liquids. *Science* **321,** 1306–1307 (2008).
3. Yamashita, M. *et al*. Highly mobile gapless excitations in a two-dimensional candidate quantum spin liquid. *Science* **328,** 1246–1248 (2010).
4. Sachdev, S. Quantum magnetism and criticality. *Nature Phys.* **4,** 173–185 (2008).
5. Nayak, C., Simon, S. H., Stern, A., Freedman, M. & Sharma, S. D. Non-Abelian anyons and topological quantum computation. *Rev. Mod. Phys.* **80,** 1083–1159 (2008).
6. Lake, B., Tennant, D. A., Frost, C. D. & Nagler, S. E. Quantum criticality and universal scaling of a quantum antiferromagnet. *Nature Mater.* **4,** 329–334 (2005).
7. Han, T.-H. *et al*. Fractionalized excitations in the spin-liquid state of a kagome-lattice antiferromagnet. *Nature* **492,** 406–410 (2012).
8. Kitaev, A. Anyons in an exactly solved model and beyond. *Ann. Phys.* **321,** 2–111 (2006).
9. Baskaran, G., Mandal, S. & Shankar, R. Exact results for spin dynamics and fractionalization in the Kitaev model. *Phys. Rev. Lett.* **98,** 247201 (2007).
10. Knolle, J., Kovrizhin, D. L., Chalker, J. T. & Moessner, R. Dynamics of a two-dimensional quantum spin liquid: signatures of emergent Majorana fermions and fluxes. *Phys. Rev. Lett.* **112,** 207203 (2014).
11. Jackeli, G. & Khaliullin, G. Mott insulators in the strong spin–orbit coupling limit: from Heisenberg to a quantum compass and Kitaev models. *Phys. Rev. Lett.* **102,** 017205 (2009).
12. Chaloupka, J., Jackeli, G. & Khaliullin, G. Kitaev–Heisenberg model on a honeycomb lattice: possible exotic phases in iridium oxides A_2IrO_3. *Phys. Rev. Lett.* **105,** 027204 (2010).
13. Kim, B. J. *et al*. Phase-sensitive observation of a spin–orbital Mott state in Sr_2IrO_4. *Science* **323,** 1329–1332 (2009).
14. Singh, Y. *et al*. Relevance of the Heisenberg–Kitaev model for the honeycomb lattice iridates A_2IrO_3. *Phys. Rev. Lett.* **108,** 127203 (2012).
15. Choi, S. K. *et al*. Spinwaves and revised crystal structure of honeycomb iridate Na_2IrO_3. *Phys. Rev. Lett.* **108,** 127204 (2012).
16. Ye, F. *et al*. Direct evidence of a zigzag spin-chain structure in the honeycomb lattice: a neutron and X-ray diffraction investigation of single-crystal Na_2IrO_3. *Phys. Rev. B* **85,** 180403(R) (2012).
17. Knolle, J., Chern, G.-W., Kovrizhin, D. L., Moessner, R. & Perkins, N. B. Raman scattering signatures of Kitaev spin liquids in A_2IrO_3 iridates with A = Na or Li. *Phys. Rev. Lett.* **113,** 187201 (2014).
18. Gretarsson, H. *et al*. Magnetic excitation spectrum of Na_2IrO_3 probed with resonant inelastic X-ray scattering. *Phys. Rev. B* **87,** 220407(R) (2013).
19. Chun, S. H. *et al*. Direct evidence for dominant bond-directional interactions in a honeycomb lattice iridate Na_2IrO_3. *Nature Phys.* **11,** 462–466 (2015).
20. Figgis, B. N., Lewis, J., Mabbs, F. E. & Webb, G. A. Magnetic properties of some iron(III) and ruthenium(III) low-spin complexes. *J. Chem. Soc. A* 422–426 (1966).
21. Fletcher, J. M. *et al*. Anhydrous ruthenium chlorides. *Nature* **199,** 1089–1090 (1963).
22. Fletcher, J. M., Gardner, W. E., Fox, A. C. & Topping, G. X-ray, infrared, and magnetic studies of α- and β-ruthenium trichloride. *J. Chem. Soc. A* 1038–1045 (1967).
23. Plumb, K. W. *et al*. α-$RuCl_3$: a spin–orbit assisted Mott insulator on a honeycomb lattice. *Phys. Rev. B* **90,** 041112(R) (2014).
24. Sandilands, L. J. *et al*. Scattering continuum and possible fractionalized excitations in α-$RuCl_3$. *Phys. Rev. Lett.* **114,** 147201 (2015).
25. Sears, J. A. *et al*. Magnetic order in α-$RuCl_3$: a honeycomb lattice quantum magnet with strong spin–orbit coupling. *Phys. Rev. B* **91,** 144420 (2015).
26. Shankar, V. V., Kim, H.-S. & Kee, H.-Y. Kitaev magnetism in honeycomb $RuCl_3$ with intermediate spin–orbit coupling. *Phys. Rev. B* **91,** 241110 (2015).
27. Majumder, M. *et al*. Anisotropic Ru^{3+} $4d^5$ magnetism in the α-$RuCl_3$ honeycomb system: susceptibility, specific heat and zero-field NMR. *Phys. Rev. B* **91,** 180401(R) (2015).
28. Sandilands, L. J. *et al*. Spin-orbit excitations and electronic structure of the putative Kitaev magnet α-$RuCl_3$. *Phys. Rev. B* **93,** 075144 (2016).
29. Kubota, Y., Tanaka, H., Ono, T., Narumi, Y. & Kindo, K. Successive magnetic phase transitions in α-$RuCl_3$: XY-like frustrated magnet on the honeycomb lattice. *Phys. Rev. B* **91,** 094422 (2015).
30. Krumhansl, J. & Brooks, H. The lattice vibration specific heat of graphite. *J. Chem. Phys.* **21,** 1663–1669 (1953).
31. Abragam, A. & Bleaney, B. *Electron Paramagnetic Resonance of Transition Ions* (Oxford Univ. Press, 1970).
32. Stevens, K. W. H. On the magnetic properties of covalent XY_6 complexes. *Proc. Phys. Soc. A* **219,** 542–555 (1953).
33. Perkins, N. B., Sizyuk, Y. & Wölfle, P. Interplay of many-body and single-particle interactions in iridates and rhodates. *Phys. Rev. B* **89,** 035143 (2014).
34. Chaloupka, J., Jackeli, G. & Khaliullin, G. Zigzag magnetic order in the iridium oxide Na_2IrO_3. *Phys. Rev. Lett.* **110,** 097204 (2013).
35. Rau, J. G. & Kee, H.-Y. Trigonal distortion in the honeyccomb iridates: proximity of zigzag and spiral phases in Na_2IrO_3. Preprint at http://arxiv.org/abs/1408.4811 (2014).
36. Rau, J. G., Lee, E. K.-H. & Kee, H.-Y. Generic spin model for the honeycomb iridates beyond the Kitaev limit. *Phys. Rev. Lett.* **112,** 077204 (2014).

37. Sizyuk, Y., Price, C., Wolfle, P. & Perkins, N. B. Importance of anisotropic exchange interactions in honeycomb iridates: minimal model for zigzag antiferromagnetic order in Na_2IrO_3. *Phys. Rev. B* **90,** 155126 (2014).
38. Katukuri, V. M. *et al*. Kitaev interactions between $j=1/2$ moments in honeycomb Na_2IrO_3 are large and ferromagnetic: insights from *ab initio* quantum chemistry calculations. *New J. Phys.* **16,** 013056 (2014).
39. Chaloupka, J. & Khaliullin, G. Hidden symmetries of the extended Kitaev–Heisenberg model: implications for honeycomb lattice iridates A_2IrO_3. *Phys. Rev. B* **92,** 024413 (2015).
40. Alpichshev, Z., Mahmood, F., Cao, G. & Gedik, N. Confinement-deconfinement transition as an indication of spin-liquid-type behavior in Na_2IrO_3. *Phys. Rev. Lett.* **114,** 017203 (2015).
41. Nasu, J., Udagawa, M. & Motome, Y. Vaporization of Kitaev spin liquids. *Phys. Rev. Lett.* **113,** 197205 (2014).
42. Nasu, J., Udagawa, M. & Motome, Y. Thermal fractionalization of quantum spins in a Kitaev model. *Phys. Rev. B* **92,** 115122 (2015).
43. Modic, K. A. *et al*. Realization of a three-dimensional spin–anisotropic harmonic honeycomb iridate. *Nature Commun.* **5,** 4203 (2014).
44. Takayama, T. *et al*. Hyperhoneycomb iridate β—Li_2IrO_3 as a platform for Kitaev magnetism. *Phys. Rev. Lett.* **114,** 077202 (2015).
45. Zschocke, F. & Vojta, M. Physical states and finite-size effects in Kitaev's honeycomb model: bond disorder, spin excitations, and NMR lineshape. *Phys. Rev. B* **92,** 014403 (2015).

Acknowledgements

Research using ORNL's HFIR and SNS facilities was sponsored by the US Department of Energy, Office of Science, Basic Energy Sciences (BES), Scientific User Facilities Division. A part of the synthesis and the bulk characterization performed at ORNL was supported by the US Department of Energy, Office of Science, Basic Energy Sciences, Materials Sciences and Engineering Division (C.A.B. and J.-Q.Y.). The work at University of Tennessee was funded in part by the Gordon and Betty Moore Foundation's EPiQS Initiative through Grant GBMF4416 (D.G.M. and L.L.). The work at Dresden was in part supported by DFG grant SFB 1143 (J.K. and R.M.), and by a fellowship within the Postdoc-Program of the German Academic Exchange Service (DAAD) (J.K.). D.L.K. is supported by EPSRC Grant No. EP/M007928/1. The collaboration as a whole was supported by the Helmholtz Virtual Institute 'New States of Matter and their Excitations' initiative. We thank B. Chakoumakos for overall support in the project, and J. Chalker, J. Rau, S. Toth, G. Khaliullin and F. Ye for valuable discussions. We thank P. Whitfield from the POWGEN beamline and Z. Gai from the CNMS facility for helping with neutron diffraction and magnetic susceptibility measurements.

Author contributions

S.E.N., A.B. and D.G.M. conceived the project and the experiment. C.A.B., A.B., L.L., J.-Q.Y., Y.Y. and D.G.M. made the sample. J.-Q.Y., L.L., A.B. and C.A.B. performed the bulk measurements, A.B., A.A.A., M.B.S., G.E.G., M.D.L. and S.E.N. performed INS measurements, A.B., S.E.N., C.A.B., M.D.L., M.B.S. and D.A.T. analysed the data. Further modelling and interpreting of the neutron scattering data was carried out by A.B., M.D.L., S.E.N., J.K., S.B., D.L.K. and R.M., where A.B., M.D.L., S.B. and S.E.N. performed SWT simulations, and J.K., S.B., D.L.K. and R.M. carried out QSL theory calculations. A.B. and S.E.N. prepared the first draft, and all authors contributed to writing the manuscript.

Additional information

Supplementary information is available in the online version of the paper. Reprints and permissions information is available online at www.nature.com/reprints. Correspondence and requests for materials should be addressed to A.B. or S.E.N.

Competing financial interests

The authors declare no competing financial interests.

Methods

Synthesis and bulk measurements. Commercial-$RuCl_3$ powder was purified in house to a mixture of α-$RuCl_3$ and β-$RuCl_3$, and converted to 99.9% phase-pure α-$RuCl_3$ by annealing at 500 °C. Single crystals of α-$RuCl_3$ were grown using vapour transport with $TeCl_4$ as the transport agent. The crystals exhibit an anisotropic mosaic for in-plane peaks, indicative of stacking faults, as shown in Supplementary Fig. 2. Samples were characterized by standard bulk techniques (see Supplementary Fig. 1). X-ray powder diffraction was carried out at room temperature using a Panalytical Empyrean diffractometer employing Cu Kα radiation.

The structure was found to be consistent with the trigonal space group $P3_112$ (No. 151), with room-temperature lattice constants $a=b=5.9783(2)$ Å, $c=17.170(1)$ Å, with $\chi^2=13.7$ and $wRp=5.16$. For $C2/m$ the corresponding fits are worse, with $a=5.982(1)$, $b=10.3530(7)$, $c=6.0611(5)$, $\beta=109.177(7)$, with $\chi^2=16.9$, $wRp=6.33$. In addition, powder neutron diffraction was carried out at 10 K. For the fit and the lattice constants at $T=10$ K refer to Supplementary Fig. 2 and Supplementary Table 2. Magnetic properties were measured with a Quantum Design (QD) Magnetic Property Measurement System in the temperature interval $1.8\,K \leq T \leq 300\,K$. Temperature-dependent specific heat data were collected using a 14 T QD Physical Property Measurement System (PPMS) in the temperature range from 1.9 to 200 K. Our measurements of the susceptibility (see Supplementary Fig. 1) are consistent with existing literature[22,25,27]. The magnetic susceptibility of powders fits a Curie–Weiss law over the range above 150 K, with a temperature intercept of $\theta \approx 32$ K and a single-ion Ru effective moment of $2.2\mu_B$. Magnetic order appears for $T \leq 15$ K, leading to a broad specific heat anomaly. The detailed specific heat of single-crystal specimens is sample dependent, but consistent with other groups[25,27,29], and shows the onset of a broad anomaly near 14 K, and a sharper peak near 8 K, possibly with additional structure between those temperatures. This complicated behaviour is a consequence of stacking faults (see main text).

Neutron diffraction. Neutron diffraction data for structural refinement on a 5.1 g powder sample of α-$RuCl_3$ were collected at the POWGEN beamline at the Spallation Neutron Source (SNS), at Oak Ridge National Laboratory (ORNL). The sample was loaded in a vanadium sample can under helium, and measured at $T \approx 10$ K. Neutron diffraction measurements to characterize the magnetic Bragg peaks in both powder and single crystals were performed at the HB-1A Fixed Incident Energy (FIE-TAX, $E_i=14.68$ meV) triple-axis instrument at the High-Flux Isotope Reactor at ORNL. For powder diffraction, 4.7 g of powder was packed into a cylindrical aluminium canister. For single-crystal diffraction, one $\sim 0.7 \times 1.0\,cm^2$, 22.5 mg crystal was attached to a flat aluminium shim using Cytop-M glue. It was then sealed with indium into an aluminium canister with helium exchange gas, then aligned and confirmed to be a single-domain sample using neutrons. This was attached to the cold finger of a 4 K closed-cycle refrigerator for performing the temperature scans.

Inelastic neutron scattering (INS). Inelastic neutron scattering of powder α-$RuCl_3$ was performed using the SEQUOIA chopper spectrometer at the SNS (ref. 46). The sample (5.3 g) was sealed at room temperature in a $5 \times 5 \times 0.2\,cm^3$ flat aluminium sample can using helium exchange gas for thermal contact. This was mounted to the cold finger of a closed-cycle helium refrigerator for temperature control. Empty can measurements were performed under the same conditions as the sample measurements. The neutron detector efficiencies were calibrated using vanadium standards, and the neutron counts were normalized to the accumulated incident proton charge. The data presented have the empty can background subtracted, and the uncertainties were calculated assuming Poisson counting statistics with conventional propagation of error calculations. Measurements were made with incident neutron energies $E_i=8$, 25 and 1,500 meV. The $E_i=8$ and 25 meV measurements were performed using the fine-resolution 100 meV Fermi chopper slit package spinning at 180 Hz and the T_0 chopper spinning at 30 Hz. The $E_i=1,500$ meV measurements used the 700 meV coarse-resolution Fermi chopper spinning at 600 Hz and the T_0 chopper spinning at 180 Hz (ref. 47). The $E_i=1,500$ meV configuration yields a calculated full-width at half-maximum (FWHM) energy resolution of approximately 97 meV at 200 meV energy transfer. The FWHM elastic energy resolution is calculated to be 0.19 and 0.64 meV for the $E_i=8$ and 25 meV configurations, respectively. Care was taken to minimize the exposure of the sample to air, and after every exposure the sample was pumped for at least 30 min to remove adsorbed moisture. Structural refinements confirmed the purity of the powder sample. Spin wave simulations were performed using SpinW codes[48] (Version 235) and used the nominal symmetric honeycomb structure for α-$RuCl_3$ (refs 21,22). The SWT powder average was performed with 3,000 random points distributed over the Brillouin zone. The Ru^{3+} form factor utilized was interpolated using the results of relativistic Dirac–Slater wave functions[49].

References

46. Granroth, G. E. *et al*. SEQUOIA: a newly operating chopper spectrometer at the SNS. *J. Phys. Conf. Ser.* **251,** 12058 (2010).
47. Abernathy, D. L. *et al*. Design and operation of the wide angular range chopper spectrometer ARCS at the SNS. *Rev. Sci. Instrum.* **83,** 15114 (2012).
48. Toth, S. & Lake, B. Linear spin wave theory for single-Q incommensurate magnetic structures. *J. Phys. Condens. Matter* **27,** 166002 (2014).
49. Cromer, D. T. & Weber, J. T. *Scattering Factors Computed from Relativistic Dirac–Slater Wave Functions* LANL REPORT LA-3056 (Los Alamos Research Library, 1964).